

Pattern Fluctuations in Transitional Plane Couette Flow

Joran Rolland · Paul Manneville

Received: 21 October 2010 / Accepted: 12 January 2011 / Published online: 26 January 2011
© Springer Science+Business Media, LLC 2011

Abstract In wide enough systems, plane Couette flow, the flow established between two parallel plates translating in opposite directions, displays alternatively turbulent and laminar oblique bands in a given range of Reynolds numbers R . We show that in periodic domains that contain a few bands, for given values of R and size, the orientation and the wavelength of this pattern can fluctuate in time. A procedure is defined to detect well-oriented episodes and to determine the statistics of their lifetimes. The latter turn out to be distributed according to exponentially decreasing laws. This statistics is interpreted in terms of an activated process described by a Langevin equation whose deterministic part is a standard Landau model for two interacting complex amplitudes whereas the noise arises from the turbulent background.

Keywords Fluid dynamics · Turbulence · Pattern formation · Jump process

1 Introduction

The main features of the transition to turbulence are well understood in systems prone to a linear instability like convection where chaos emerges at the end of an instability cascade. A much wilder transition is observed in wall-bounded shear flows for which the laminar and turbulent regimes are both possible states at intermediate values of the Reynolds number R , the natural control parameter, whereas no linear instability mechanism is effective. A direct transition can take then place via the coexistence of laminar and turbulent domains in physical space. Two emblematic cases are the pipe flow and plane Couette flow (PCF), the simple shear flow developing between two parallel plates translating in opposite directions. Both of them are stable against infinitesimal perturbations for all values of R and become turbulent only provided sufficiently strong perturbations are present. In both cases, strong hysteresis is observed and, upon decreasing R , the turbulent state can be maintained down to a value R_g . Above R_g , turbulence remains localised in space, in the form of turbulent puffs in pipe flow and turbulent patches in PCF. A striking property of PCF or counter-rotating

J. Rolland (✉) · P. Manneville
Laboratoire d'Hydrodynamique de l'École Polytechnique, 91128 Palaiseau, France
e-mail: joran.rolland@ladhyx.polytechnique.fr

cylindrical Couette flow (CCF) is the spatial organisation of turbulence in alternatively turbulent and laminar oblique bands that takes place in large enough systems in a specific range of Reynolds numbers [1, Chap. 7]. This regime was studied in depth at Saclay by Prigent *et al.* [2]. It can be obtained by decreasing the Reynolds number continuously from featureless turbulence below R_t , the Reynolds number above which the flow is uniformly turbulent, or triggered from laminar flow by finite amplitude perturbations above R_g , the Reynolds number below which laminar flow is expected to prevail in the long time limit. A similar situation is observed in pipe flow but things are complicated by the global downstream advection so that the existence of a threshold R_t above which turbulence is uniform is still a debated matter. In contrast for PCF, the pattern is essentially time-independent and can be characterised by two wavelengths λ_x and λ_z in the streamwise and spanwise direction, x and z respectively,¹ or equivalently by a wavevector $\mathbf{k} = (k_x, k_z)$ with $k_{x,z} = 2\pi/\lambda_{x,z}$. From symmetry considerations, two orientations are possible, corresponding to two possible combinations $(k_x, \pm k_z)$. Whereas a single orientation is present sufficiently far from R_t so that either mode $(k_x, +k_z)$ or mode $(k_x, -k_z)$ is selected, patches of one or the other orientation have been reported to fluctuate in space and time when R approaches R_t from below [2, Figs. 2 and 3]. The main features of the bifurcation diagram could then be accounted for at a phenomenological level by an approach in terms of Ginzburg–Landau equations subjected to random noise featuring the small-scale turbulent background.

This patterning was reproduced by Duguet *et al.* [3] using fully resolved numerical simulations in an extended system of size comparable with that of the Saclay apparatus but the computational load was so heavy that a statistical study of the upper transitional range was inconceivable. Earlier, Barkley & Tuckerman [4] also succeeded in obtaining the bands by means of fully resolved simulations with less computational burden but using narrow elongated domains aligned with the pattern's wavevector. By construction, the fluctuating domain regime could not be obtained, whereas a re-entrant featureless turbulence regime, called 'intermittent' was obtained closer to R_t .

In our previous work on this problem, we first showed that full numerical resolution was not necessary to obtain realistic patterning but that a good account of the long range streamwise correlation of velocity fluctuations was essential [5]. This next incited us to consider reduced-resolution simulations in systems of sizes sufficient to contain at least an elementary cell (λ_x, λ_z) of the pattern [6], thus avoiding the orientation constraint inherent in the Barkley–Tuckerman approach. Here, we expand our previous work to focus on pattern fluctuations in the upper part of the PCF's bifurcation diagram when R approaches R_t from below, taking the best possible use of the inescapable resolution lowering to perform long duration simulations, so as to obtain meaningful statistics about the dynamics of this regime.

Systems considered in our numerical experiment, to be described in Sect. 2, produce patterns with a few wavelengths. In the neighbourhood of R_t , fluctuations manifest themselves as orientation changes in time instead of the spatiotemporal evolution of well-ordered patches. It turns out that episodes of well-formed pattern between two orientation changes can be identified reliably, so that the lifetimes of such episodes can be measured and their average determined as a function of R . The Langevin approach initiated by Prigent *et al.* in [2] was resumed in [6] as providing an appropriate framework to interpret our numerical results. Orientation fluctuations were taken into account but their detailed statistical properties left aside, which are the subject of the present paper.

¹In the case of CCF, the pattern is time-independent in a frame that rotates at the mean angular velocity and the axial (azimuthal) direction corresponds to the spanwise (streamwise) direction.

In the context of pattern formation, the Langevin/Fokker–Planck approach has a long history, dating back to the 1970's when it was applied to convecting systems [7]. Noise of thermal origin is however extremely weak so that the region of parameter space where the system is sensitive to this noise is exceedingly narrow [8] and nontrivial effects can be observed only in very specific conditions [9]. When applying the approach to the description of the bifurcation from featureless turbulence to pattern in shear flows, Prigent *et al.* [2] implicitly took for granted that the noise intensity was an adjustable parameter linked to the turbulent background at $R > R_t$. Here we extend the analysis started in [6] within this conceptual framework, the subject of Sect. 3, and analyse simulation results presented in Sect. 2.4 in the light of this theory. We conclude in Sect. 4 by discussing how well this approach is suited to describe mode competition and intermittent re-entrance of featureless turbulence [4, 6] and, more generally, how the noisy temporal dynamics of coherent modes can hint at the spatio-temporal nature of transitional wall-bounded flows and explain the exponentially decreasing probability distributions of residence times or decay times often observed in this field [12].

2 Conditions of the Numerical Experiment

2.1 Numerical Procedure

Direct numerical simulation (DNS) of the incompressible Navier–Stokes equations in the geometry of PCF are performed using Gibson's open source code CHANNELFLOW [10] that assumes no-slip boundary conditions at the plates driving the flow and in-plane periodic boundary conditions. The parallel plates producing the shear are placed at a distance $2h$ from each other in the wall-normal direction y , they move at speeds $\pm U$ in the streamwise direction x , z labelling the spanwise direction. The length unit is h , the velocity unit U , the time unit h/U , and the Reynolds number $R = Uh/\nu$, where ν is the kinematic viscosity of the fluid. The problem is completely specified when the in-plane dimensions L_x and L_z of the set-up are chosen. The perturbation to the laminar flow $\mathbf{U} = y\hat{\mathbf{x}}$ is noted \mathbf{u} , so that \mathbf{u}^2 is the local Euclidean distance to the base flow squared. Periodic in-plane boundary conditions allow the definition of the wave-vectors $k_{x,z} = 2\pi n_{x,z}/L_{x,z}$, where the wavenumbers $n_{x,z}$ are integers. Without loss of generality, we can assume $n_x \geq 0$.

The resolution of the simulation is fixed by the number N_y of Chebyshev polynomials used to represent the wall-normal dependence, and the numbers $N_{x,z}$ of collocation points used to evaluate the nonlinear terms in the pseudo-spectral scheme of integration of the Navier–Stokes equations. The number of Fourier modes involved in the simulation is then $2N_{x,z}/3$, owing to the 3/2-rule applied to de-alias the velocity field. The computational load necessary to obtain meaningful results in sufficiently wide domains with fully resolved simulations is unrealistically heavy. Accordingly, we take advantage of our previous work devoted to the validation of *systematic under-resolution* as a *modelling strategy* [5]. In that work, we showed that qualitatively excellent and quantitatively acceptable results could be obtained by taking $N_y = 15$ and $N_{x,z} = 8L_{x,z}/3$. The price to be paid for the resolution lowering was apparently just a downward shift of the range $[R_g, R_t]$ in which the bands are obtained, but everything else was preserved, including wavelengths. Of course, as far as resolution is concerned, the finest is the best on a strictly quantitative basis but we do not expect that the observed trends and our conclusions be sensitive to our rules to fix N_y and $N_{x,z}$.

2.2 Orientation Fluctuations

In this article we consider domains able to contain a pattern with one or two elementary cells, i.e. $L_{x,z} = |n_{x,z}| \lambda_{x,z}$ where $n_x = 1$ or 2 and $n_z = \pm 1$ or ± 2 . According to [2], in PCF wavelength λ_x is found to be approximately equal to 110 over the whole range $[R_g, R_t]$, while wavelength λ_z varies as a function of R in the range [40, 85]. These observations serve us to fix the size of the systems that we are going to consider below. As shown in [6], the specificity of such systems is to convert the spatio-temporal evolution of fluctuating domains observed in the neighbourhood of R_t into the temporal evolution of coherent patterns characterised by the amplitudes of the corresponding fundamental Fourier modes; possible orientation changes are associated with changes of sign of the spanwise wavenumbers. Close enough to R_t , there is also some probability that featureless turbulence, the state that prevails for $R > R_t$, be observed transiently, which is akin to the intermittent regime identified in [4]. In contrast, in the lowest part of the transitional range, close to R_g , the orientation remains frozen as expected for well-formed steady oblique bands. We first illustrate this phenomenon using snapshots of \mathbf{u}^2 in Figs. 1 and 2. The left and centre panels of Fig. 1 display well-oriented patterns or ‘pure states’ showing the organised cohabitation of laminar and turbulent flow; an example of defective pattern or ‘mixed state’ without much spatial organisation is shown in the right panel. (Orientation defects between well-oriented domains require wider systems to be clearly identified as such.) Figure 2 similarly displays snapshots of \mathbf{u}^2 obtained in a narrower but longer system.

Typically, during long-lasting simulations at given $L_{x,z}$ and R , the flow displays a pure pattern for some time, then experiences a brief defective stage, and next recovers a pure state, possibly with different orientation or/and wavelength, and so on. The spatial organisation of the pattern is detected *via* the Fourier transform of the perturbation velocity field $\hat{\mathbf{u}}$. It turns out that most of the information about the modulation is encoded in the amplitude of the dominant wavenumber [2, 6, 11]. We consider time series of

$$m^2(n_x, n_z, t) = \frac{1}{2} \int_{-1}^{+1} |\hat{u}_x(n_x, y, n_z, t)|^2 dy, \tag{1}$$

which thus characterises a flow pattern with wavelengths $(\lambda_x, \lambda_z) = (L_x/n_x, L_z/|n_z|)$ and orientation given by the sign of n_z . In the present study, we focus on the amplitude of the

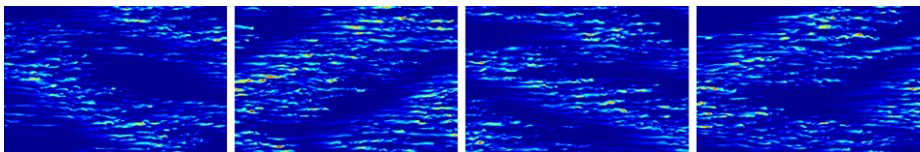


Fig. 1 (Color online) Snapshots of \mathbf{u}^2 in the plane $y = -0.57$ for $R = 315$ in a system of size $L_x \times L_z = 128 \times 84$. From left to right: one band pure state with each of the two possible orientations ($n_x = 1, n_z = +1$) or ($n_x = 1, n_z = -1$), two band pure state ($n_x = 1, n_z = +2$), and mixed or defective pattern. Deep blue corresponds to laminar flow

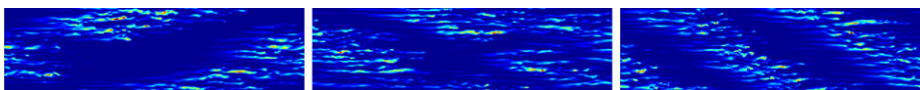


Fig. 2 Snapshots of \mathbf{u}^2 in the plane $y = -0.57$ for $R = 290$ in a system of size $L_x \times L_z = 170 \times 48$. From left to right: ($n_x = 1, n_z = -1$), ($n_x = 1, n_z = +1$), and ($n_x = 2, n_z = +1$)

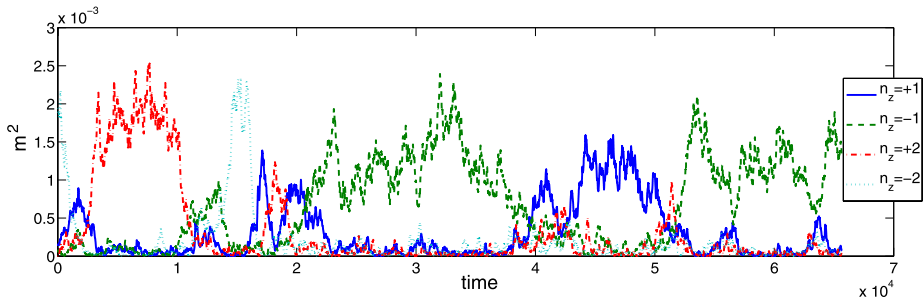


Fig. 3 Time series of $m^2(t)$ for several wave numbers $n_z = \pm 1, \pm 2$ for $R = 315$ in a system of size $L_x \times L_z = 128 \times 84$

turbulence modulation in the flow and not on its phase, i.e. on the position of the pattern in the system, which was shown to be a random function of time [6].

An example of such time series is displayed in Fig. 3. A pure pattern stage corresponds to a single $m(n_x, n_z)$ fluctuating around a non zero value, the other $m(n'_x, n'_z)$ remaining negligible. For instance the pattern keeps wave-number $n_z = +2$ from $t = 3 \times 10^3$ to $t = 10^4$. The defective stage corresponds to $m(n_x, n_z)$ decaying to zero while another one $m(n'_x, n'_z)$ grows. Wavenumbers (n'_x, n'_z) may be different from (n_x, n_z) , in which case there is an effective change of the orientation if $|n'_z| = |n_z|$ or a change of wavelength (sometimes combined with an orientation change) if $|n'_z| \neq |n_z|$. In Fig. 3, a change of orientation takes place at time $t = 4 \times 10^4$ ($n_z = -1 \rightarrow +1$), a change of wavelength at time $t = 1.7 \times 10^4$ ($n_z = -2 \rightarrow +1$), the pattern with $n_z = +1$ growing back from a defective stage at time $t = 4.3 \times 10^4$. Most of the time there is no ambiguity about the value of n involved so that we shall use simplified notations, i.e. just m or m_{\pm} instead of $m(n_x, \pm n_z)$, as often as possible.

Except very close to R_t , pure state intermissions last long and defective episodes are short, so that series of lifetime T_i of well-oriented lapses can be defined from recording simulations of duration sufficient to make reliable statistics.

2.3 Lifetime Computations

Orientation and wavelength fluctuations are best characterised by lifetimes distributions. Beforehand, we have to define a systematic method to detect the beginning and the end of pure pattern episodes from the m^2 time series. This is done by using two thresholds: one, s_1 , for the start of a pure pattern episode and the other, s_2 , for its termination, see Fig. 4 (top). The fast growth of m^2 makes it easy to choose s_1 and the results are not much sensitive to its exact value. In contrast, detecting the decay is more problematic. This will be discussed in detail after the presentation of a typical result obtained by assuming that the difficulty has been properly resolved.

For practical reasons, we use a byproduct of the cumulated probability density function (PDF) Q :

$$Q(T) = \frac{\#\{T_i \geq T\}}{\#\{T_i\}} = 1 - \frac{\#\{T_i \leq T\}}{\#\{T_i\}}.$$

Empirical distributions obtained in an experiment with $L_x = 110$ and $L_z = 32$ for $R = 330$ are displayed in Fig. 5. They are obtained from the time series, a small part of which is shown in Fig. 4, distinguishing $n_z = \pm 1$ from $n_z = \pm 2$. Since, for symmetry reasons,

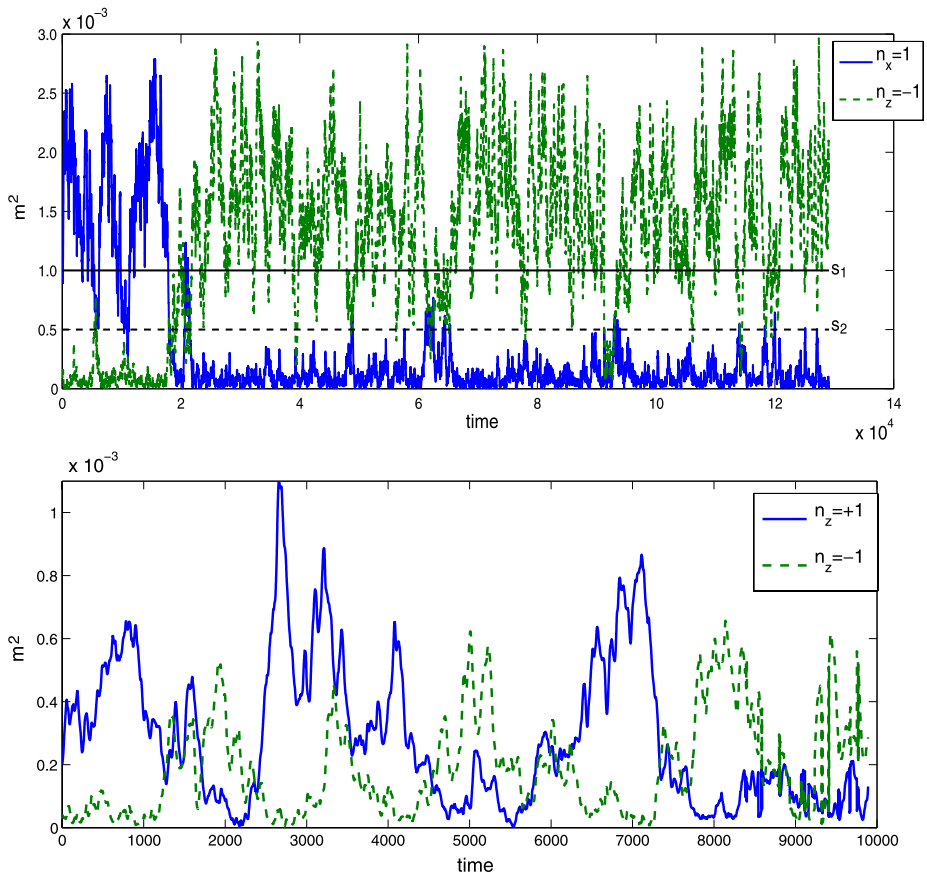
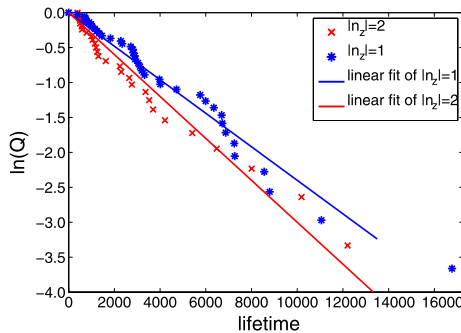


Fig. 4 Time series of m^2 for $n_z = \pm 1$ at $R = 330$ (top) and $R = 345$ (bottom). The two horizontal lines in the top panel locate threshold s_1 (full line) and s_2 (dashed line). Close to R_t , bottom panel, orientation fluctuations are short-lived and much smaller, rendering the detection of well-oriented episodes more difficult

Fig. 5 Logarithm of Q (right) for $L_x \times L_z = 128 \times 84$, $R = 315$, computed with $s_1 = 0.001$, $s_2 = 0.005$, for both wave numbers $|n_z| = 1$ and $|n_z| = 2$. We have about 40 events for $|n_z| = 1$ and about 20 events for $|n_z| = 2$



the two orientations are supposed to have identical distributions, we sum over the \pm in each case. The semi-logarithmic coordinates used to represent $Q(T)$ suggest exponentially decreasing variations, which makes orientation changes look like deriving from a Poisson

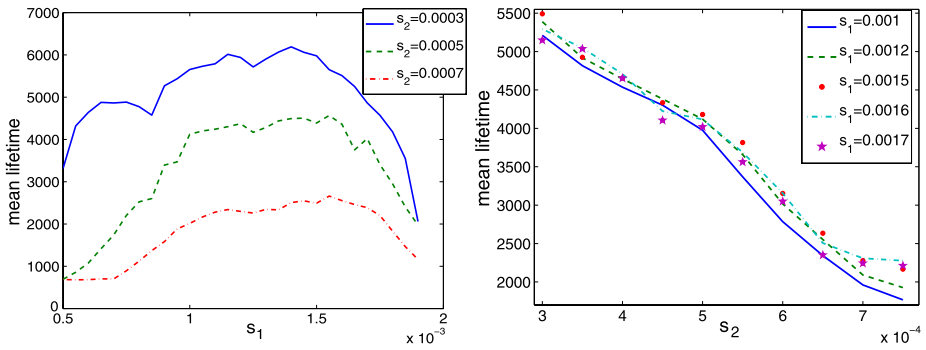


Fig. 6 Mean lifetimes functions of s_1 given s_2 (left) and of s_2 given s_1 (right). $R = 315$ and system size $L_x \times L_z = 128 \times 84$, $|n_z| = 1$

process. Assuming that they are indeed in the form $\exp(-T/\langle T \rangle)$, we can obtain the mean lifetime $\langle T \rangle$ from the plain arithmetic average of the lifetime series. $\langle T \rangle$ can also be obtained by fitting the empirical cumulated distribution against an exponential law or its logarithm against a linear law. In addition to raw data, Fig. 5 displays the second kind of fits for $|n_z| = 1$ and 2. These three different estimates are close to each other provided that the lifetime series comprise sufficiently large numbers of events. An average of these three values will be used to define the mean lifetime and the corresponding unbiased standard deviation will give an estimate of the “error” for each lifetime series.

Let us now come to the problem of the sensitivity of $Q(T)$ to the value of the thresholds s_1 and s_2 used to determine the lifetimes of the pure pattern episodes. In Fig. 6 (left) the mean lifetime $\langle T \rangle$ displays a clear plateau as a functions of s_1 . The width of this plateau does not depend on s_2 though its value depends on it. The existence of this plateau is easily seen to be related to the fast growth of m when the pattern sets in: m always goes through most of the values corresponding to the plateau in a very short time. In practice, for $10^{-3} \leq s_1 \leq 1.5 \times 10^{-3}$ the very same episodes are detected whatever the precise value of s_1 . That the plateau value still depends on s_2 just expresses that the duration of the detected episodes are modified in the same way due to changes in the detection of their termination. Of course, when s_1 is taken too large, some less-well ordered episodes escape detection or are detected too late, which artificially decreases the mean. On the other hand, if s_1 is taken too small, the “signal” gets lost in the “noise”: a large number of brief noisy excursions are detected as relevant ordered episodes, again decreasing the mean.

The variation of the mean lifetime with s_2 is completely different as seen in Fig. 6 (right). Here, $\langle T \rangle$ varies roughly linearly with s_2 in a wide interval above the noise level ($\sim 3 \times 10^{-4}$, see Fig. 4):

$$\langle T \rangle(s_2) \simeq a(1 - bs_2).$$

Coefficient $b = 1000 \pm 100$ does not vary significantly over the cases that we have considered. This dependence fully explains the change of plateau value in plots of $\langle T \rangle$ as a function of s_1 . Coefficient a , corresponding to $\langle T \rangle$ extrapolated toward $s_2 = 0$ however still depend on R and the geometry. Henceforth, we define this extrapolated value as the relevant average lifetime $\langle T \rangle$, which will be supported by the theoretical considerations to be developed in the next section.

The observed dependence of $\langle T \rangle$ on s_2 can be explained by the fact that the decay of a pure pattern is much more gradual than its growth, which causes significant differences

when the duration of an episode is measured, leading to a decrease of $\langle T \rangle$ as s_2 increases since the termination of the episode is detected earlier. A second reason why the mean lifetime increases as s_2 decreases arises from the fact that some excursions are not counted as decay events. In physical space, this corresponds to an irregular and slow disorganisation of turbulence, contrasting with the fast installation of the pattern. In fact $\langle T \rangle$ cannot be obtained otherwise than by extrapolation of threshold s_2 to zero, as will be discussed in Sect. 3.3.

2.4 DNS Results

The two systems sizes, $L_x \times L_z = 128 \times 64$ and 110×32 , already considered in our previous work [5, 6] are studied here over the whole range of Reynolds numbers where the pattern exists at the chosen numerical resolution, $R \in [R_g, R_t] = [275, 345]$. Orientation fluctuations are systematically found close enough to R_t , see Cases 1 & 2 below.

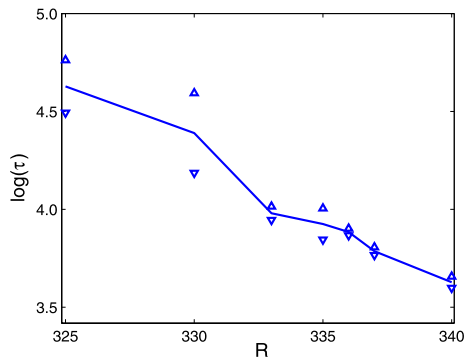
In addition, wavelength fluctuations can take place when the size of the system is too far away from resonating with the pattern's elementary cell $\lambda_x^{\text{opt}} \times \lambda_z^{\text{opt}}$, where 'opt' means 'optimal', in a sense to be defined below in Sect. 3.1. Orientation and wavelength fluctuations are observed at $R = 315$ for $L_x = 128$, $L_z = 84$ and 90, and for $L_x = 110$, $L_z = 84$, meaning that both $|n_z| = 1$ and $|n_z| = 2$ are competitive for $L_z = 84$ or $L_z = 90$. In contrast, lifetimes of single mode patterns are extremely long for $L_z < 84$ and $L_z > 90$, meaning that $L_z < 84$ is optimal for $|n_z| = 1$ and $L_z > 90$ is optimal pour $|n_z| = 2$. Orientation and wavelength fluctuations are similarly present in several other circumstances, at lower Reynolds number $R = 272$ and $R = 275$ for $L_x \times L_z = 110 \times 32$, as well as at $R = 290$ for $L_z = 48$ and $L_x = 80$ or at $R = 330$ for $L_x = 90, 140$, and 150.

Case 1: $L_x = 128$, $L_z = 84$, $R = 315$, wavelength fluctuations Several experiments under the same protocol have been performed, using different initial conditions. Integration times ranged from 5×10^4 to $10^5 h/U$. A large enough ensemble of lifetimes has been sampled, both for $|n_z| = 1$ and $|n_z| = 2$, allowing us to compute the corresponding order parameters M —the conditional time averages of $m(t)$ as defined in (1)—with sufficient accuracy. Snapshots corresponding to this aspect ratio are displayed in Fig. 1, a typical part of the corresponding time series is shown in Fig. 3. For $|n_z| = 1$ and $|n_z| = 2$, we obtain $M_1 = 0.033 \pm 0.001$ and $M_2 = 0.038 \pm 0.001$, respectively. From the lifetime distributions in Fig. 5, we get $\tau_1 = 8100 \pm 200$ and $\tau_2 = 3800 \pm 100$. The fact that $M_1 < M_2$ is not surprising and is understood in term of optimal wavelength (Sect. 3.1, $\lambda_z^{\text{opt}} \simeq 39$ at $R = 315$ [6]). The reason why one has $\tau_1 > \tau_2$ is however not clear.

Case 2: $L_x = 110$, $L_z = 32$, variable R , orientation fluctuations A thorough account of the behaviour of M and the re-entrance featureless turbulence has been given in [6]. Here, lifetimes are computed for Reynolds number ranging from $R = 325$ to $R = 340$. Below $R = 325$, the lifetimes are so long that a small number of events is observed despite the length of time series used ($> 2 \times 10^5$), which forbids the determination of τ as a meaningful average (Fig. 10). Above $R = 340$, a clear separation of time scales is lacking, which now forbids the definition of lifetimes of individual events, compare the two panels in Fig. 4.

Figure 7 displays the variation of the average lifetime τ with R , showing that it increases by a factor of 10 as R decreases from $R = 340$, which is somewhat below $R_t = 355$, down to $R = 325$ below which it is too long to be measured reliably. "Error bars" suggested by up and down triangles in Fig. 7 correspond to the unbiased standard deviation of the three estimates for τ mentioned earlier.

Fig. 7 Mean lifetime τ as a function of R for $L_x \times L_z = 110 \times 32$ (log scale)



3 Conceptual Framework and Application to DNS Results

3.1 The Landau–Langevin Model

Prigent *et al.* proposed to consider the turbulent bands as resulting from a conventional pattern formation problem described at lowest order, from symmetry arguments, by two coupled cubic Ginzburg–Landau equations, one for each band orientation, further subjected to noise featuring the turbulent background above R_t . The slowly varying part of the velocity field component away from the laminar profile can be written as

$$u_x = A_+(\tilde{x}, \tilde{z}, \tilde{t})e^{ik_x^c x + ik_z^c z} + A_-(\tilde{x}, \tilde{z}, \tilde{t})e^{ik_x^c x - k_z^c z} + cc,$$

where $A_{\pm} \in \mathbb{C}$ are the amplitude fields accounting for the two modulation waves, and \tilde{x} , \tilde{z} and \tilde{t} are slow variables [1]. Then, following this approach, we assume

$$\tau_0 \partial_{\tilde{t}} A_{\pm} = (\epsilon + \xi_x^2 \partial_{\tilde{x}\tilde{x}}^2 + \xi_z^2 \partial_{\tilde{z}\tilde{z}}^2) A_{\pm} - g_1 |A_{\pm}|^2 A_{\pm} - g_2 |A_{\mp}|^2 A_{\pm} + \alpha \zeta_{\pm}, \tag{2}$$

the quantity $\epsilon = (R_t - R)/R_t$ measures the relative distance to the threshold² R_t , τ_0 is the ‘natural’ time scale for pattern formation, $\xi_{x,z}$ are streamwise and spanwise correlation lengths, g_1 and g_2 are the self-coupling and cross-coupling nonlinear coefficients, and α the strength of the noise ζ_{\pm} supposed to be a centred Gaussian process with unit variance. The strength α of the noise is expected to grow smoothly with R , regardless of the existence of the pattern since the local intensity of the turbulence is empirically not directly correlated to the amplitude and phase of the modulation A_{\pm} . The tilde variables describe the long-wave modulations to an ideal pattern with critical wavelengths $\lambda_{x,z}^c$ to which correspond critical wavevectors $k_{x,z}^c = 2\pi/\lambda_{x,z}^c$, the term critical referring to the most unstable wave vector near $R = R_t$. The systems that we consider have periodic boundary conditions placed at distances $L_{x,z}$. Fourier analysis then leads to characterise the pattern by wavevectors $\mathbf{k} = (k_x, k_z)$, with $k_{x,z} = 2\pi n_{x,z}/L_{x,z}$. It is assumed that the wave numbers obtained during a given experiment will be the integers that will be as close as possible of $n_{x,z}^c = L_{x,z}/\lambda_{x,z}^c$. Furthermore, our systems can accommodate a small number of cells of size (λ_x, λ_z) so their modes are well isolated [1, Chap. 4]. Assuming that a single pair $(n_x, \pm n_z)$ is involved, the partial differential equation (2) is turned into an ordinary differential equation for $A(n_x, \pm n_z)$ simply

²The existence of a well defined threshold in this system is attested by the behaviour of the turbulent fraction and spatially averaged kinetic energy which display a marked change of slope at R_t [6].

denoted $A_{\pm} \equiv A_{\pm}^r + i A_{\pm}^i$, close enough to R_t [6]:

$$\tau_0 \frac{d}{dt} A_{\pm} = \tilde{\epsilon} A_{\pm} - g_1 |A_{\pm}|^2 A_{\pm} - g_2 |A_{\mp}|^2 A_{\pm} + \alpha \zeta_{\pm}, \tag{3}$$

where $\tilde{\epsilon} = \epsilon - \xi_x^2 \delta k_x^2 - \xi_z^2 \delta k_z^2$ controlling the linear stability of these modes, is evaluated for $\delta k_{x,z} = k_{x,z} - k_{x,z}^c$ with the relevant $k_{x,z} = 2\pi n_{x,z} / L_{x,z}$, as well as the nonlinear coefficients $g_{1,2}$ ($\in \mathbb{R}$ because the pattern does not drift, at least in the absence of noise). Coefficient α is the effective strength of the noise affecting the mode that we consider. Equation (3) can be written as deriving from a potential:

$$\tau_0 \frac{d}{dt} A_{\pm}^r = - \frac{\partial \mathcal{V}}{\partial A_{\pm}^r} + \alpha \zeta_{\pm},$$

with

$$\mathcal{V} = -\frac{1}{2} \tilde{\epsilon} (|A_+|^2 + |A_-|^2) + \frac{1}{4} g_1 (|A_+|^4 + |A_-|^4) + \frac{1}{2} g_2 |A_+|^2 |A_-|^2. \tag{4}$$

Usually, when making use of phenomenological equations such as (2), one relies on values of critical wavevectors k^c that are computed once and for all from some linear stability theory and further introduced in the perturbation expansions solving the nonlinear wavelength selection problem beyond the threshold [13]. Here the theory is not developed enough to have such a definition and such an evaluation of nonlinearly selected ‘optimal’ wavevectors far enough from threshold. Accordingly, in (3) we introduce values of $\tilde{\epsilon}$ that do not make reference to some explicit computation involving measured values of ϵ and $\xi_{x,z}$ but values that are just estimates consistent with the empirically determined optimal wavelengths. In the same way, we keep the cubic Landau expressions (3), neglecting higher order terms that would introduce too many little-constrained parameters, without deeper insight into the problem.

The stable fixed points of the deterministic part of (3) were shown to correspond to the permanent state of the pattern and the additive noise term seen to account for fluctuations quite well by solving the corresponding Fokker–Planck equation [6]. The stationary probability distribution for the moduli $|A_{\pm}| = A_{\pm}^m$ was obtained in the form:

$$\Pi(A_+^m, A_-^m) = Z^{-1} A_+^m A_-^m \exp(-2\mathcal{V}/\alpha^2), \quad Z = \int A_+^m A_-^m \exp(-2\mathcal{V}/\alpha^2) dA_+^m dA_-^m. \tag{5}$$

The time behaviour of A_{\pm}^m is easily discussed by considering the shape of \mathcal{V} within the stochastic process framework. Two limiting cases can be identified, depending on whether $\tilde{\epsilon}$ is $\mathcal{O}(1)$ or $\ll 1$. In the first case, excursions from the neighbourhood of the minima of \mathcal{V} are rare; the lifetime of an ordered episode can be defined as the average time necessary for the system to go from the neighbourhood of a minimum to the potential’s saddle. It is expected to increase with the height of the potential barrier, i.e. as parameter $\tilde{\epsilon}$ grows, and to fall off as α increases. The lack of symmetry between the growth and the decay of a pattern has then a clear explanation when $\tilde{\epsilon}$ is large: The growth corresponds to the system falling from the neighbourhood of the saddle into one of the wells; even in the presence of noise, this evolution is fast and mostly deterministic. In contrast, the decay corresponds to the system slowly climbing toward the saddle against the deterministic flow, driven by the sole effect of noise. In the opposite limit, when $\tilde{\epsilon}$ approaches zero, the definition of a lifetime no longer makes sense since the characteristic times for growth and decay become of the same order of magnitude.

3.2 Orientation Lifetimes from the Model

Orientation changes and associated lifetimes are analysed in terms of *first passage time* and *escape from metastable states* [14]. The distribution of lifetimes is anticipated to be Poissonian as expected from a jump process controlled by an activation “energy”. In a simplified one-dimensional version of potential \mathcal{V} [14, Chap. 11, Sects. 2, 6–7], if the well is deep enough, within a parabolic approximation the mean escape time, the average time necessary to go from a well to another, is given by

$$\tau/\tau_0 = \frac{2\pi}{\sqrt{\mathcal{V}''_w|\mathcal{V}''_s|}} \exp\left(2\frac{\mathcal{V}_s - \mathcal{V}_w}{\alpha^2}\right), \tag{6}$$

where ‘w’ stands for ‘well’ and ‘s’ for ‘saddle’; $\mathcal{V}_{w,s}$ are the values of the potentials at the corresponding points and $\mathcal{V}''_{w,s}$ the values of the second order derivatives of the potential with respect to the variable at these points. The derivation of this formula shows that τ is dominated by the time spent around the saddle. In our two dimensional system with potential (4), at lowest order in α the coordinates of the well and saddle points are:

$$(A_{\pm}^w, A_{\mp}^w) = \left(\sqrt{\tilde{\epsilon}/g_1}, 0\right) \quad \text{and} \quad (A_+^s, A_-^s) = \left(\sqrt{\tilde{\epsilon}/(g_1 + g_2)}, \sqrt{\epsilon/(g_1 + g_2)}\right)$$

and the corresponding values of the potential:

$$\mathcal{V}_w = -\tilde{\epsilon}^2/4g_1 \quad \text{and} \quad \mathcal{V}_s = -\tilde{\epsilon}^2/2(g_1 + g_2).$$

The second derivatives have to be replaced by the eigenvalues of the Hessian matrix of \mathcal{V} computed at these points:

$$H_w = \begin{pmatrix} 2\tilde{\epsilon} & 0 \\ 0 & \tilde{\epsilon}(g_2/g_1 - 1) \end{pmatrix} \quad \text{and} \quad H_s = \frac{2\tilde{\epsilon}}{g_2 + g_1} \begin{pmatrix} g_1 & g_2 \\ g_2 & g_1 \end{pmatrix}.$$

At point ‘w’, H_w is diagonal and the eigen-direction pointing to point ‘s’ has eigen-value $\tilde{\epsilon}(g_2/g_1 - 1)$. At point ‘s’, H_s is diagonal in the basis $\{(1, 1), (1, -1)\}$ and has eigenvalues $\{2\tilde{\epsilon}, 2\tilde{\epsilon}(g_1 - g_2)/(g_1 + g_2)\}$. The unstable eigen-direction correspond to the second one which is negative ($g_2 > g_1$). Inserting these values in (6), we obtain:

$$\tau/\tau_0 = \frac{2\pi\sqrt{2}}{\tilde{\epsilon}} \frac{\sqrt{g_1(g_1 + g_2)}}{g_2 - g_1} \exp\left(\frac{\tilde{\epsilon}^2}{2\alpha^2 g_1} \frac{g_2 - g_1}{g_1 + g_2}\right). \tag{7}$$

In its exponential factor, this formula points out an “energy” scale $\tilde{\epsilon}^2/g_1$ to be compared to the characteristic noise energy α^2 which play the role of the Boltzmann energy in thermal problems. It also shows that, especially when g_2 is larger but comparable to g_1 , the noise energy has to remain small enough because the parabolic approximation which underlies the formula assumes sufficiently deep wells. The main difference between the one and two dimensions cases are in the shape of the “energy landscape”, corrections are therefore expected to be multiplicative and not depend on the value of $\tilde{\epsilon}$.

3.3 Simulation of the Model

For the deterministic part of (3) we use a simple first-order implicit Euler algorithm, while the additive noise $\alpha\zeta(t)$ is treated as a Gaussian random variable with standard deviation

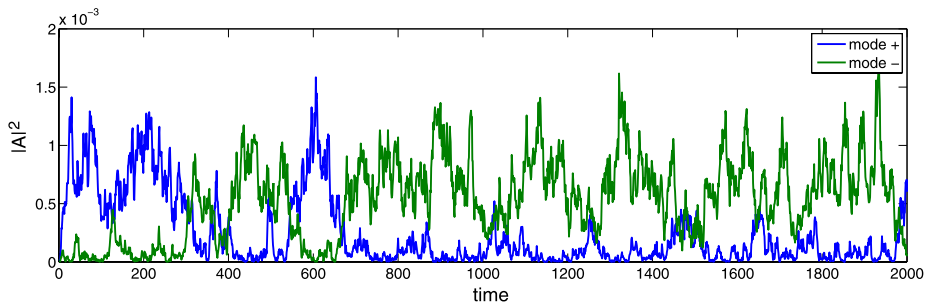


Fig. 8 Typical time series from model (3), for a set of parameters corresponding to the Navier–Stokes DNS, $\tilde{\epsilon} = 0.05$, $g_1 = 60$, $g_2 = 120$, $\alpha = 0.002$ [6]

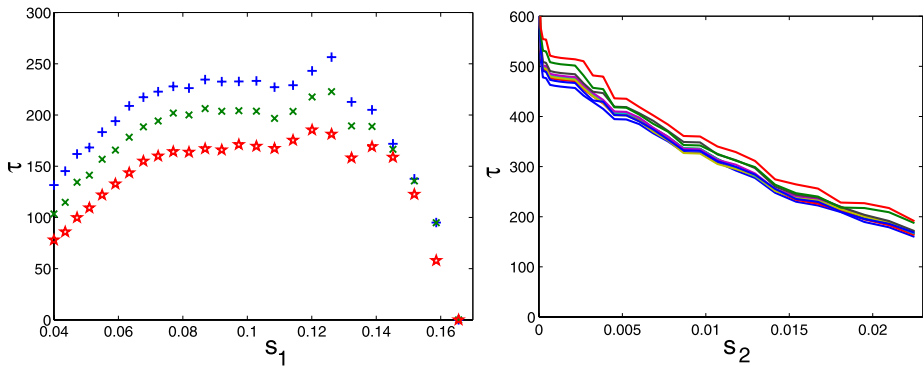
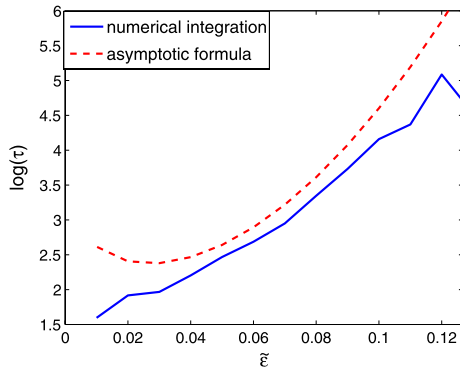


Fig. 9 Mean lifetime τ , extracted from the model as a function of s_1 , for $s_2 = 0.0163$, 0.0193 , and 0.0225 (left) and as a function of s_2 for several s_1 ranging from 0.0784 to 0.1296 (right). $\tilde{\epsilon} = 0.075$, $g_1 = 1$, $g_2 = 2$, $\alpha = 0.002$

$\alpha\sqrt{dt}$ at each time step. The model is integrated over a range of $\tilde{\epsilon}$, given g_1 , g_2 (several values), and α (assumed constant). The time series of $|A_{\pm}|^2$ displayed in Fig. 8 are indeed reminiscent of those obtained by numerical integration of Navier–Stokes equations (Figs. 3 and 4): pure states at the bottom of the wells correspond to $|A_-|^2$ fluctuating around 0 and $|A_+|^2$ away from 0, or the reverse. Large excursions can lead to a change of the dominant orientation. These excursions are more likely to occur when $\tilde{\epsilon}$ is decreased.

Lifetimes have been computed in the same way as for Fig. 6. The dependence of the mean lifetimes on thresholds $s_{1,2}$ is displayed in Fig. 9. A neat plateau is obtained for $s_1 \in [0.075, 0.115]$ for different values of s_2 (Fig. 9, left), which corresponds to the trajectory getting away from the saddle. Extremes values of s_1 lead to bad estimates of τ for the same reasons as stated before. As to threshold s_2 , an orientation change has taken place when the trajectory goes beyond the saddle, while a pure state corresponds to one amplitude large and the other at the noise level. We have thus to detect the change from large to small for one or the other amplitude. It is extremely difficult to detect the precise passage at the saddle, since it is dominated by the time spent in that region, contribution from the two sides of the saddle point having the same weight. On the contrary the passage from one state to another leaves no doubt as to its definition. Therefore, we prefer to compute the mean first passage time from one well to another, which is obtained in our simulation by the extrapolation at $s_2 = 0$. Approximating the curves in Fig. 9 (right) by linear functions $\tau = a(1 - bs_2)$, one

Fig. 10 $\log(\tau)$ as a function of $\tilde{\epsilon}$ for $g_1 = 60, g_2 = 120, \tilde{\alpha} = 0.002$; the model was integrated over 10^5 time units



finds that the slope b depends on $\tilde{\epsilon}$ and s_1 only weakly; the value of τ retained is then the one given by the extrapolation $s_2 = 0$, i.e. coefficient a . Improving the definition of τ with approximations better than the linear one has not been found necessary. The general expression of the mean first passage time gives no hint as to the quantitative behaviour on the distance to the second well s_2 , although it shows the same qualitative behaviour as seen in Figs. 6 (right) and 9 (right). In Fig. 10 (semilog coordinates), the lifetime τ measured in this way is compared to the asymptotic expression from the theory (7) as a function of $\tilde{\epsilon}$. It can be seen that the asymptotic formula is not valid for the smallest values of $\tilde{\epsilon}$, when the wells are not longer deep enough for the approximation to be valid, similarly to what is found in the DNS close to R_t . The values given by this formula for small values of $\tilde{\epsilon}$, especially around and below the minimum it predicts at $\tilde{\epsilon} = \alpha \sqrt{g_1(g_2 + g_1)/(g_2 - g_1)}$, cannot be trusted. For large $\tilde{\epsilon}$, the lifetime computed from the simulation saturates because it becomes of the order of the total integration time so that only a few events smaller than this total time can be recorded. Accordingly the long time tail of the distribution is badly sampled with an under-representation of lifetimes larger than the average expected from the theory. In Fig. 10, the numerical and the asymptotic estimates of the mean lifetimes are seen to differ by a constant of order unity, which is attributed to the one-dimensional character of the approximation.

3.4 Generalisation

This approach can be extended to wavelength fluctuations. When the size (L_x, L_z) of the system is such that it ‘hesitates’ between two pairs of modes $(n_x, \pm n_z)$ and $(n'_x, \pm n'_z)$, we introduce two supplementary amplitudes $A(n'_x, \pm n'_z)$ that we denote B_{\pm} for short and, extending notations straightforwardly with primes for quantities related to B_{\pm} , we arrive at:

$$\tau_0 \frac{d}{dt} A_{\pm} = \tilde{\epsilon} A_{\pm} - g_1 |A_{\pm}|^2 A_{\pm} - g_2 |A_{\pm}|^2 A_{\pm} + g_3 (|B_{\pm}|^2 + |B_{\mp}|^2) A_{\pm} + \alpha \zeta_{\pm}, \quad (8)$$

$$\tau_0 \frac{d}{dt} B_{\pm} = \tilde{\epsilon}' B_{\pm} - g'_1 |B_{\pm}|^2 B_{\pm} - g'_2 |B_{\pm}|^2 B_{\pm} + g'_3 (|A_{\pm}|^2 + |A_{\mp}|^2) B_{\pm} + \alpha' \zeta'_{\pm}, \quad (9)$$

where $\tilde{\epsilon}$ and $\tilde{\epsilon}'$ as well as the nonlinear coupling constants $g_{1,2,3}, g'_{1,2,3}$ and even the effective noise intensities α, α' may differ since they relate to pure patterns with different $\delta k_{x,z} = k_{x,z} - k^c_{x,z}$. A first guess would be to assume the primed and non-primed variables equal, which would bring us immediately back to the previous approach with an effective potential, wells, saddles, and potential barriers, leading to estimates for the different lifetimes involved.

It is not clear how the case of turbulence re-entrance (the intermittent regime of [4]) would fit this framework but it is well described by a PDF with three peaks [6] corresponding to a probability potential with three wells and thus hopefully amenable to a similar treatment with a similar output.

These generalisations have not been worked out in detail numerically since they introduces a discouragingly large number of parameters to be fitted against the experiments and from which we would learn little, owing to their phenomenological basis. Only the case involving a single pair of modes was examined in Sect. 3.3 above, mostly in order to validate the procedure followed to determine lifetimes in Sect. 2.3.

4 Summary and Conclusion

In this paper, numerical simulations of the Navier–Stokes equation in plane Couette flow configuration have been performed in a range of Reynolds numbers where the transition to turbulence happens in the form of oblique bands. Systems with sizes fitting a few elementary cells $\lambda_x \times \lambda_z$ of the pattern have been considered. These sizes are much larger than the minimal flow unit which allows the reduction of the transition problem to a temporal process familiar to chaos theory [12]. Accordingly, the considered systems are able to display the first manifestations of a genuinely spatiotemporal dynamics *via* patterning. Following the patterns in time, we showed that they experience orientation and wavelength fluctuations in the upper part of the range of transitional Reynolds numbers $[R_g, R_t]$. A systematic procedure to detect the start and the termination of well-oriented episodes was defined, leading to the observation of exponentially decreasing distributions for their lifetimes (Fig. 5).

A consistent interpretation scheme was then provided by adapting the noisy Ginzburg–Landau model proposed in [2] to our case, transforming the original stochastic PDE into a Landau–Langevin stochastic ODE. Besides supporting the procedure used to determine lifetimes, the approach directly leads to the determination of probability distributions for the patterned states from the shape of the potential obtained by solving the corresponding Fokker–Planck equation, as already suggested in [2, Fig. 19]. The variation of the patterns' mean lifetimes is thus linked to the relative distance to threshold and noise intensity through an asymptotic formula involving the “energy” barrier between wells corresponding to the different well-oriented states in competition. Ingredients in the relative distance to threshold $\tilde{\epsilon}$ which is a function of both the Reynolds number and the optimal wavelength, are amply sufficient to explain most of the dependence of the mean lifetimes as functions of R , $L_{x,z}$, and the spontaneous appearance of defects separating patches of well-oriented patterns close enough to R_t in larger aspect-ratio systems as illustrated in Fig. 11 and seen in the experiments [2].

In order to explain the occurrence of exponentially decreasing lifetime distributions, the theory of dynamical systems appeals to the sensitivity to initial conditions of trajectories visiting a homoclinic tangle [12]. Here, the modelling that fits well our observations implies that exponential distributions arise from some jump random process [14]. As soon as the size of the system is much larger than the minimal flow unit (for which the temporal behaviour

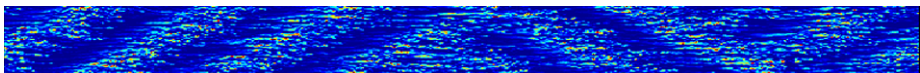


Fig. 11 Orientation defect spontaneously appearing in the flow for $R = 340$ in a domain of size $L_x \times L_z = 660 \times 48$

inherent in low dimensional dynamical systems is relevant), a spatiotemporal perspective becomes in order, and the jumps in question can easily be associated to the local chaotic dynamics of pieces of streaks and streamwise vortices involved in the self sustaining process of turbulence [15]. This local chaotic dynamics would then be responsible for the wandering of the global system through some “energy” landscape with wells and saddles. With system sizes of the order of the elementary pattern cell $\lambda_x \times \lambda_z$, this wandering amounts to orientation and/or wavelength changes. Extending these views to larger systems would then explain the statistical properties of fluctuating laminar-turbulent patches observed in the upper transitional range close enough to R_t [2].

Whereas the origin of the noise introduced in the description is understandable from chaos at the local (microscopic) scale, it remains however to understand why the coexistence of laminar and turbulent flow takes the form of oblique bands at the global (macroscopic) scale, i.e. to justify the Ginzburg–Landau approach from the first principles rather than taking it as an educated phenomenological guess.

References

1. Manneville, P.: *Instabilities, Chaos and Turbulence*, 2nd edn. Imperial College Press (2010)
2. Prigent, A., Grégoire, G., Chaté, H., Dauchot, O.: Long-wavelength modulation of turbulent shear flow. *Physica D* **174**, 100–113 (2003)
3. Duguet, Y., Schlatter, P., Henningson, D.S.: Formation of turbulent patterns near the onset of transition in plane Couette flow. *J. Fluid Mech.* **650**, 119–129 (2010)
4. Barkley, D., Tuckerman, L.: Computational study of turbulent laminar patterns in Couette flow. *Phys. Rev. Lett.* **94**, 014502 (2005)
5. Manneville, P., Rolland, J.: On modelling transitional turbulent flows using under-resolved direct numerical simulations. *Theor. Comput. Fluid Dyn.* doi:10.1007/s00162-010-0215-5. In press
6. Rolland, J., Manneville, P.: Ginzburg–Landau description of laminar-turbulent oblique bands in transitional plane Couette flow. *Eur. Phys. J. B*. Submitted
7. Graham, R.: Hydrodynamics fluctuations near the convection instability. *Phys. Rev. A* **10**, 1762–1784 (1974)
8. Hohenberg, P., Swift, J.: Effects of additive noise at the onset of Rayleigh–Bénard convection. *Phys. Rev. A* **46**, 4773–4785 (1992)
9. Scherer, M., Ahler, G., Hörner, F., Rehberg, I.: Deviation from linear theory for fluctuations below the super-critical primary bifurcation to electroconvection. *Phys. Rev. Lett.* **85**, 3754–3760 (2000)
10. Gibson, J.: <http://www.channelflow.org/>
11. Barkley, D., Dauchot, O., Tuckerman, L.: Statistical analysis of the transition to turbulent-laminar banded patterns in plane Couette flow. *J. Phys. Conf. Ser.* **137**, 012029 (2008)
12. Eckhardt, B., Faisst, H., Schmiegel, A., Schneider, T.M.: Dynamical systems and the transition to turbulence in linearly stable shear flows. *Philos. Trans. R. Soc. A* **366**, 1297–1315 (2008)
13. Cross, M.C., Hohenberg, P.C.: *Rev. Mod. Phys.* **65**, 851–1112 (1993)
14. Van Kampen, N.G.: *Stochastic Processes in Physics and Chemistry*. North-Holland, Amsterdam (1990)
15. Waleffe, F.: On a self-sustaining process in shear flows. *Phys. Fluids* **9**, 883–900 (1997)